NIST Author Manuscript

NIST Author Manuscript

NIST Author Manuscript

Author Manuscript

Accepted for publication in a peer-reviewed journal

NIST National Institute of Standards and Technology • U.S. Department of Commerce

Published in final edited form as:

J Electrochem Soc. 2019 ; 166(1): .

Effect of Chloride Concentration on Copper Deposition in Through Silicon Vias

T. M. Braun[*,z], **D. Josell**, **M. Silva**, **J. Kildon**, **T. P. Moffat**[**]

Materials Science and Engineering Division, National Institute of Standards and Technology, Gaithersburg, Maryland 20899, USA

Abstract

Bottom-up Cu deposition in metallized through silicon vias (TSV) depends on a co-adsorbed polyether–Cl^- suppressor layer that selectively breaks down within recessed surface features. This work explores Cu deposition when formation of the suppressor blocking layer is limited by the flux of Cl^-. This constraint leads to a transition from passive surfaces to active deposition partway down the via sidewall due to coupling between suppressor formation and breakdown as well as surface topography. The impact of Cl^- concentration and hydrodynamics on the formation of the suppressor surface phase and its potential-dependent breakdown is examined. The onset of suppression breakdown is related to the local Cl^- coverage as determined by the adsorption isotherm or transport limited flux. A two-additive co-adsorption model is presented that correlates the voltammetric potential of suppression breakdown with the depth of the passive-active transition during TSV filling under conditions of transport limited flux and incorporation of Cl^-. The utility of potential waveforms to optimize the feature filling process is demonstrated. At higher Cl^- concentrations (80 μmol/L), sidewall breakdown during Cu deposition occurs near the bottom of the via followed by a shift to bottom-up growth like that seen at higher Cl^- concentrations.

Extreme bottom-up Cu filling of through silicon vias has been demonstrated using $CuSO_4$-H_2SO_4 and $Cu(CH_3SO_3)_2$-CH_3SO_3H electrolytes that include a combination of halide and polyether additives to selectively inhibit metal deposition.[1–8] Halide adsorption by itself leads to acceleration of the copper deposition rate while polyether co-adsorption on the halide adlayer gives rise to significant inhibition of copper deposition by limiting access of Cu^{2+}_{aq} to the metal surface.[1–26] Electroanalytical,[1–26] gravimetric microbalance,[14,15] ellipsometry[18] and vibrational spectroscopy[27,28] studies unambiguously demonstrate that halide adsorption is required for co-adsorption of an effective polyether suppressor layer. Co-adsorption involves factors from the multiplicity of halide-polyether binding sites,[24] to halide perturbation of interface water structure that makes it more hydrophobic favoring polyether adsorption,[28] to a possible role of Cu^+ as an ether-halide binding agent.[9,11,27]

This is an open access article distributed under the terms of the Creative Commons Attribution Non-Commercial No Derivatives 4.0 License (CC BY-NC-ND, http://creativecommons.org/licenses/by-nc-nd/4.0/), which permits non-commercial reuse, distribution, and reproduction in any medium, provided the original work is not changed in any way and is properly cited. For permission for commercial reuse, please email: oa@electrochem.org. [DOI: 10.1149/2.0341901jes]

[z] tbraun4213@gmail.com.

[*]Electrochemical Society Member.

[**]Electrochemical Society Fellow.

NIST Author Manuscript NIST Author Manuscript NIST Author Manuscript

Upon polarization to negative potentials the inhibition breaks down and the electrode bifurcates into active plating versus passive regions that subsequently yields significant voltammetric hysteresis.[1–9] The magnitude of positive feedback and bifurcation is sensitive to the additive concentrations and applied potential and is correlated with negative differential resistance (S-NDR) that may require correction for resistive electrolyte losses to be revealed.[1,3–6,24] The slow temporal response of metal cation and additive transport as compared to the rapid electrode polarization underlies the bifurcation.[1,3,5,6,29,30] With topographically engineered electrodes the breakdown process can be tuned to localize deposition to the most recessed regions and thereby optimized to give bottom-up via filling.

Positive feedback between suppressor breakdown and metal deposition is intrinsic to the filling process. Suppression breakdown can involve incorporation of the suppressing additives into the growing film that yields a concentration gradient within the unfilled volume of the recessed feature.[3,5,8,16] Additional and/or alternative avenues proposed for disruption of the halide-polymer suppressor layer include reduction of a Cu^+ halide-ether binding agent,[9,11,17] potential driven order-disorder transitions in the underlying halide adlayer[31] and disruption of the polymer adsorption process by the metal deposition process itself.[1,4,21–26] The filling process is also known to be quite sensitive to the initial conditions.[1,3,5,6] Quantitative linkage of electroanalytical measurements, processing and feature filling is presently a topic of significant interest.

In models of additive incorporation, the initial conditions as well as the kinetics of adsorption and consumption collectively impact the metal deposition rate and location of the passive-active breakdown and subsequent morphological and microstructural evolution as seen in systems including Cu and beyond.[3,5,32–36] When deposition is localized to the bottom surface, void-free bottom-up via filling is possible while sidewall breakdown results in either superconformal, conformal or subconformal deposition depending on the extent of the additive and metal cation depletion. Bottom-up Cu deposition in the halide-polyether system is accompanied by significant metal cation depletion at the growth front.[1,3,5,37] In contrast, when additive breakdown occurs at the via sidewalls it is primarily associated with significant additive depletion at the passive-active transition.[3,5,32–36] In the absence of significant metal depletion conformal deposition in the active regions yields horseshoe shaped deposits as, for a fixed applied potential, the location of the sidewall transition does not advance significantly with time.[32–34] However, as the aspect ratio of the actively plating region increases metal ion depletion eventually sets in and further deposition becomes sub-conformal.[32–36] Importantly, implementation of an appropriate potential, or current, waveform can enable the position of the sidewall passive-active transition to be systematically advanced toward the free surface to substantially fill the features.[32–36]

Experimentally, bottom-up growth has been observed for specific formulations of the two-component halide-polyether suppressor chemistry for Cu[1–7] while the sidewall passive-active breakdown process has been detailed for Ni,[32,33] Co[34] and Au[35,36] based on a single polyethyleneimine suppressor. Metallurgical analysis reveals the impact of preferential additive incorporation on microstructural evolution at the location of the passive-active transition.[32–36] Finally, it is noteworthy that mixed feature filling behavior has been observed, with an initial period of sidewall breakdown followed by bottom-up filling in Cu

NIST Author Manuscript NIST Author Manuscript NIST Author Manuscript

deposition from an electrolyte with a low polyether suppressor concentration.[6] In this case the process was quite sensitive to the initial conditions that involved transport-limited arrival of the suppressor at the via bottom. Further advances in understanding of surfactant mediated growth processes, including the connection with microstructural development, requires comprehensive additive mass balance analysis.

Because suppression of Cu electrodeposition derives from co-adsorption of halide and polyether, the present work explores the role of Cl^- concentration, (0 to 80) μmol/L, in TSV filling at a fixed polyether concentration of 40 μmol/L. The effort complements recent experiments on the effect of polyether concentration, (0.25 to 25) μmol/L, on TSV filling at fixed Cl^- concentration of 1 mmol/L.[6] Voltammetric analysis and feature filling simulations are performed based on a simple two additive model for polyether co-adsorption where the polyether only adsorbs on the Cl^- covered surface as defined by its fractional coverage without concern for the detailed steric arrangements required, e.g., for multisite polymer binding, etc. For dilute Cl^- concentrations, breakdown of suppression and activation of the metal deposition is dominated by the loss of adsorbed halide to incorporation within the growing deposits. The rate constants for Cl^- adsorption and consumption are derived from fitting breakdown of the passive state on the first negative-going voltammetric cycle. As with previous work,[1,3,5,6] the applied potentials selected for feature filling experiments lie within the hysteretic voltammetric window and time dependent feature filling experiments are directly compared with simulations.

Experimental

The electroanalytical and feature filling experiments were conducted at room temperature in a cell containing 40 mL of 1 mol/L $CuSO_4$ and 0.5 mol/L H_2SO_4. A poloxamine suppressor, ethylenediamine tetrakis (propoxylate-*block*-ethoxylate) tetrol, $(PEO_4PPO_{12})_2ED(PPO_{12})PEO_4)_2$ ($M_{n\ avg} \approx 3600$, Tetronix 701, Aldrich) was used with the concentration fixed at 40 μmol/L. Solutions with different chloride concentration were made using aliquots from a master solution of 5 mmol/L NaCl dissolved in 18 MΩ · cm water. Sparging with argon between electrochemical measurements was used to reduce parasitic currents associated with dissolved oxygen. A Hg/Hg_2SO_4/saturated K_2SO_4 reference electrode (SSE) was connected to the working electrode compartment via a fritted bridge filled with a saturated solution of K_2SO_4. The platinum counter electrode was held in a frit-separated cell immersed within the main cell.

Voltammetry was performed using a 0.5 cm diameter (area 0.20 cm^2) rotating disk electrode (RDE) machined from oxygen-free, high conductivity copper that was freshly polished on 1200 grit silicon carbide paper prior to each experiment. All voltammetry shown was collected at 2 mV/s with 70% iR compensation based on the measured high frequency cell resistance $R \approx 6.5\ \Omega$. Currents measured in the electroanalytical experiments are converted to current densities based on the projected RDE area. However, because suppression breakdown and metal deposition in the additive-containing electrolytes often entails bifurcation of the electrode into active and passive regions, the actual current density is ill-defined beyond suppression breakdown.[1]

NIST Author Manuscript
NIST Author Manuscript
NIST Author Manuscript

Feature filling was performed using 3 mm × 12 mm wafer fragments patterned with ≈ 56 μm deep TSV of annular cross-section (provided by IBM) having a 1 μm thick Cu seed on the field and a lesser amount on the side walls and TSV bottoms. The TSV substrates rotated about one end from a Pt spindle during deposition, like a helicopter blade, the patterned surface facing up to give definition to the metal ion and additive transport. Based on the ≈ 1 cm distance between the features and rotational axis for most of the imaged TSVs, the 100 rpm (200**π** rad/min) rotation rate corresponds to an estimated 10 cm/s flow rate over the surface. Pre-wetting with ethyl alcohol was used to displace air bubbles that were otherwise trapped in the TSV prior to Cu deposition. Following immersion, the specimens were rotated while poised at a potential of –0.40 V (an overpotential of ≈ 20 mV based on the measured reversible potential of ≈ –0.38 V) for two minutes to mix the electrolyte with the alcohol in the TSV. The specified deposition potential was applied immediately thereafter. In contrast to voltammetry, no iR compensation was used in the feature filling experiments.

Electroanalytical Measurements

Linear sweep voltammetry probing the rate of metal deposition as a function of Cl^- concentration in the poloxamine containing electrolyte reveals a systematic increase in suppression manifesting as decreased current and expansion of the potential range of the passivated state. For a RDE rotation rate of 100 rpm, a modest negative shift of the current density-voltage trace occurs for Cl^- concentrations up to 15 μmol/L (Figure 1a). However, suppression increases by over 180 mV for Cl^- concentrations of 20 μmol/L and higher. The potential threshold for breakdown of the suppressed state shifts negative monotonically with halide concentration over the entire range. When the RDE rotation rate is increased 4-fold, corresponding to 2-fold decrease in the hydrodynamic boundary layer thickness, an increase in suppression is evident for lower Cl^- concentrations, e.g. 120 mV for 6 μmol/L, while only a minor increase in polarization is evident for higher concentrations. The slope of the current density following the breakdown of suppression is limited by the uncompensated portion of the iR potential drop associated with the cell resistance R_{cell}. Post-experiment correction of the applied potential for potential drop across the electrolyte with higher Cl^- concentrations (e.g., the > 20 mV positive shift for current density > 10 mA/cm^2 given the uncompensated ≈ 2 Ω) would reveal the additive derived S-NDR.

A closer examination of the Cl^- dependence of suppression breakdown on hydrodynamics is shown in Figure 2. The extent of inhibition is particularly sensitive for the most dilute chloride concentrations, consistent with formation of the suppressor layer being limited by the flux of Cl^-. The sensitivity weakens for Cl^- concentrations above 20 μmol/L, indicating a saturated Cl^- coverage is established by the time the voltammetric sweep reaches the breakdown potential. The further shift of the breakdown potential with increasing Cl^- concentration reflects the potential dependence of the halide adsorption isotherm and/or related structural phase transitions. Parameterization of the suppressor breakdown threshold using the potential (E) at 1 mA/cm^2 as a function of Cl^- concentration is consistent with a slope of $dE/d\log[Cl^-] \approx -60$ mV/dec as suggested in Figure 3. The deviations at lower Cl^- concentration and lower rotation rate reflect transport limitations on halide adsorption, and the range of congruence with the isotherm behavior is thus extended to lower Cl^- concentration for higher rotation rate. Previous work on Cl^- adsorption on Cu(110) surfaces

NIST Author Manuscript NIST Author Manuscript NIST Author Manuscript

in acid media reveals a structural phase transition in the same potential range whose desorption peak potential, E_p, changes as $dE_p/\log[Cl^-] \approx -61$ mV/dec, the data and fit also shown in Figure 3.[31] The concentration dependence of the onset of suppression breakdown is linked to a fixed Cl^- coverage or related structural transition in the halide layer in accord with the adsorption isotherm. In contrast to the electroanalytical threshold measurements, the localized suppressor breakdown associated with feature filling occurs at slightly more positive potentials, *vida infra*. Accordingly, an understanding of the spatiotemporal variations of the Cl^- concentration within the recessed via geometry and their impact on both the formation of the halide-polyether suppressor layer and its disruption by the metal deposition process itself is needed. The accelerated deposition associated with the positive-going branch of the hysteretic voltammetry is a useful probe that convolves contributions from simple halide desorption, desorption stimulated by metal deposition and/or its consumption by incorporation within the growing deposit. However, the non-uniform growth across the work piece associated with the bifurcation into passive and active zones combined with limited microstructural information makes the extraction of robust kinetic parameters difficult.

The analysis presented here utilizes a simple construct wherein suppression provided by polyether coverage is limited by chloride coverage, with both species following Langmuir adsorption kinetics normalized by the respective saturation coverage values. Metal deposition disrupts suppression by removal of Cl^- that involves some combination of desorption and/or incorporation into the growing deposit. Herein chloride incorporation at a rate proportional to the local current density and adsorbate coverage is considered.

Accordingly, evolution of the fractional chloride coverage θ_{Cl} is described by

$$\frac{d\theta_{Cl}}{dt} = k_{Cl}^{+} C_{Cl}(1 - \theta_{Cl}) - k_{Cl}^{-} \theta_{Cl} v \quad [1]$$

Where k_{Cl}^{+} is the adsorption rate constant, C_{Cl} is the concentration at the electrolyte/deposit interface, k_{Cl}^{-} is the incorporation rate constant and v is deposition rate. Likewise, the fractional polymer coverage θ_P is described by

$$\frac{d\theta_P}{dt} = k_P^{+} C_P(\theta_{Cl} - \theta_P) - k_P^{-} \theta_P v \quad [2]$$

where the polyether, P, is only able to adsorb on halide covered sites and thereby implicitly subject to the requirement that θ_P cannot exceed θ_{Cl} through adsorption.

The mass balance between additive diffusion across the boundary layer and its adsorption onto the surface is expressed for chloride by

$$D_{Cl} \frac{C_{Cl}^{o} - C_{Cl}}{\delta} = \Gamma_{Cl} k_{Cl}^{+} C_{Cl}(1 - \theta_{Cl}) \quad [3]$$

using the bulk concentration C_{Cl}^{o} and similarly for suppressor by

$$D_P \frac{C_P^o - C_P}{\delta} = \Gamma_P k_P^+ C_P(\theta_{Cl} - \theta_P)\,. \quad [4]$$

Values for the areal densities of sites Γ_i, additive diffusion coefficients D_i, and boundary layer thickness δ (scaling with the rotation rate as $\omega^{-0.5}$) were estimated from the literature.[38–40] Γ_{Cl} was taken to be 1.62×10^{-5} mol/m^2 that corresponds to half that of a smooth Cu (111) surface. Γ_P was taken to be 9.2×10^{-8} mol/m^2 based on the molecule lying flat like a pancake at the interface. This value is based on the correlation between surface pressure behavior and the number of EO and PO groups comprising various poloxamines.[40] Data for a similar poloxamine, Tetronic 901, indicate that with a strong increase in surface pressure the polymer could be compressed toward a brush conformation that is unlikely to exceed 2.5×10^{-7} mol/m^2. The diffusion coefficient for the polymer was estimated to be 1×10^{-10} m^2/s based on literature data for similar molecular weights of polyethylene glycol.[41–43] Metal ion depletion across the boundary layer was accounted for by balancing the ion flux across the boundary layer, weighted by the molar volume, with the deposition rate

$$\Omega D_{Cu} \frac{C_{Cu}^o - C_{Cu}}{\delta} = \upsilon \quad [5]$$

The deposition rate is assumed to be a linear function of the suppressor coverage and metal ion concentration at the interface, thus

$$\upsilon(\theta_P, \eta) = \frac{\Omega}{nF} \frac{C_{Cu}}{C_{Cu}^o}\left[j_{\theta\,=\,0}(1 - \theta_P) + j_{\theta\,=\,1}\theta_P\right] \quad [6]$$

The current density on unsuppressed ($j_{\theta=0}$) and suppressed ($j_{\theta=1}$) surfaces is only associated with metal deposition and thus directly reflects the growth velocity, v, using Faraday's constant (F = 96485 C/mol), the ionic charge n, and the molar volume Ω of solid Cu. This simple form captures suppression arising from the polyether coverage as limited by chloride coverage. The current density ($j_{\theta=0,1}$) is assumed to exhibit the conventional exponential dependence on overpotential η (relative to the reversible potential of ≈ –0.38 V estimated from the current onset in the voltammetry)

$$j_{\theta\,=\,0,\,1} = j_{\theta\,=\,0,\,1}^o e^{-\frac{\alpha_{\theta\,=\,0,\,1} F\eta}{RT}} \quad [7]$$

where the back reaction has been neglected due to the high overpotentials used in the feature filling experiments. As defined using Eq. 6, the exchange current density $j_{\theta\,=\,0,\,1}^o$ for the bare, θ = 0, and fully inhibited, θ = 1, surface is for bulk metal ion concentration C_{Cu}^o at the interface. The values of $j_{\theta\,=\,1}^o$ and $\alpha_{\theta=1}$ were obtained by fitting the suppressed negative-going sweeps at higher Cl^- concentrations up to the onset of suppression breakdown. Logarithmic plots were used due to the very low current densities. The kinetics of metal deposition on polymer-free surfaces are also a function of the halide coverage. However, for

NIST Author Manuscript NIST Author Manuscript NIST Author Manuscript

simplicity in the present work a single set of $j^o_{\theta=0}$ and $\alpha_{\theta=0}$ is used. Finer distinction between various surfaces will await a more sophisticated modeling effort.

With the voltammetry acquired compensating for 70% of the iR potential drop, the simulations incorporate the remaining 30% uncompensated resistance to enable the direct comparison to experiment shown in Figure 2. Fitting the voltammograms to obtain k_i^+ and k_i^- for the additives, (i = Cl^- and P, Tetronic 701 polyether) was performed by integrating Eqs. 1 and 2 for $\theta_i(t)$ subject to Eqs. 3 through 6, with a focus on capturing the dependence of the suppression breakdown potential on the Cl^- concentration and RDE rotation rate. The parameters used to fit the voltammetry are given in Table I along with the resulting k_i^+ and k_i^- values. The fit obtained for suppression breakdown over the range of Cl^- concentrations (4 μmol/L to 80 μmol/L) and RDE rotation rates (25 rpm to 1600 rpm) is reasonable. The model underestimates suppression at the lowest chloride concentrations (4 μmol/L, 6 μmol/L, and 10 μmol/L), most likely due to minor chloride contamination in the $CuSO_4$ source material that is not inconsistent with the specified maximum impurity level. As a result, the estimated fits assume an additional 1 μmol/L Cl^- from contamination across the range explored in Figure 2. Although the model overestimates suppression for 80 μmol/L Cl^-, the proposed mechanism for co-adsorption of polyether and chloride captures the voltammetric trends across a wide range of experimental conditions. Both the cell resistance and metal ion transport have insignificant impact on fitting the voltammetric onset of suppression breakdown as the currents are small. For concentration at or below 80 μmol/L Cl^-, fitting of the RDE voltammetric breakdown can be captured by a range of coupled k_P^+ and k_P^- values. Importantly, this range includes the values that were previously used in one component polymer suppressor models that were able to capture conditions for bottom-up filling in 1 mmol/L Cl^- containing electrolytes (see Figure 5 in Ref. 3 and Figure 6c in Ref. 5).[3,5]

Finite Element Computational Methods

Finite element method (FEM) computations are performed in the 2D axisymmetric configuration depicted in Figure 4 imposing symmetry at the centerline of the annular via. The electrochemical cell is assumed to be a parallel plate working-counter electrode configuration with the reference point also serving as the counter electrode such that the cell resistance R_{cell} is related to electrolyte conductivity κ, reference-to-working electrode distance L and cell radius R_C through

$$R_{cell} = \frac{L}{\kappa \pi R_c^2} \quad [8]$$

The value for L (0.25 cm) was chosen to yield simulated cell resistance for a planar electrode area of 0.36 cm^2 (i.e., the dimensions of the patterned specimens) equal to the approximate 4.5 Ω cell impedance obtained experimentally. The overpotenial, η, that drives the electrodeposition reaction at the metal/electrolyte interface is referenced to the reversible Nernst potential for the reaction such that the applied potential, V_{app}, at the working electrode surface is comprised of

NIST Author Manuscript NIST Author Manuscript NIST Author Manuscript

NIST Author Manuscript

NIST Author Manuscript

NIST Author Manuscript

$$V_{app} = \eta + \phi + E_{rev} \quad [9]$$

where the potential field ϕ within the electrolyte captures potential drop from the reference due to electrolyte resistivity (i.e., $\phi = 0$ at the reference), and $E_{rev} = -0.38$ V is the estimated reversible potential for Cu deposition based on the measured open circuit potential. Initially ϕ is set to zero throughout the volume. Then the workpiece is poised at −0.40 V to simulate the experimental conditions used to allow the electrolyte to mix with the pre-wetted ethanol filled vias. After a dwell time of 120 s the applied potential was stepped to the deposition potential of interest.

The concentration and ionic flux N_i of each species in the electrolyte is defined by the Nernst-Planck equation capturing both Fickian diffusion and electromigration, such that the evolution of concentration is given by

$$\frac{dC_i}{dt} = -\nabla \cdot \overrightarrow{N}_i = -\nabla \cdot \left(-z_i u_{m,i} F C_i \nabla \phi - D_i \nabla C_i\right) \quad [10]$$

with charge z_i and its mobility $u_{m,i}$ calculated by the Einstein relation

$$u_{m,i} = \frac{D_i}{RT} \quad [11]$$

Ionic migration in the electrolyte assumes full dissociation of $CuSO_4$ intoCu^{2+} and SO_4^{2-}, H_2SO_4 into H^+ and SO_4^{2-}, and NaCl into Na^+ and Cl^-. The core of the Tetronic 701 suppressor may be protonated but is taken to be neutral in the present transport calculations.[44] Diffusion coefficients listed in Table I for Cu^{2+}, SO_4^{2-}, H^+, Na^+, and Tetronic 701 are taken or estimated from literature sources[38–43] whereas the diffusion coefficient for Cl^- was a fitting parameter estimated within the range of physically reasonable values from the voltammetry in Figure 2.

Due to the high concentration of supporting electrolyte (0.5 mol/L H_2SO_4) and estimated electrolyte conductivity (15.26 S/m),[1] potential variation in the solution due to ionic gradients is assumed to be negligible, permitting potential in the electrolyte to be defined by Laplace's equation

$$\nabla^2 \phi = 0 \quad [12]$$

with current density j associated with the ionic flux through the electrolyte given by ohms law

$$\overrightarrow{J} = -\kappa \nabla \phi \quad [13]$$

and the zero-flux condition on the side of the cell imposed by requiring

$$\frac{\partial \phi}{\partial r} = 0 \quad [14]$$

NIST Author Manuscript NIST Author Manuscript NIST Author Manuscript

The local current density at the surface of the deposit, related to η (and thus to ϕ) by Eq. 7, is equated to the Cu^{2+} flux onto the deposit (surface normal $\hat{n}$) according to

$$\frac{1}{nF}\overrightarrow{J}_{Cu}\cdot\hat{n} = -\left(z_{Cu}u_{m,Cu}FC_{Cu}\nabla\phi + D_{Cu}\nabla C_{Cu}\right)\cdot\hat{n} \quad [15]$$

The zero-flux condition of the chemical species in solution on the side of the cell is imposed by requiring

$$\frac{\partial C_i}{\partial r} = 0 \quad [16]$$

for each, with bulk concentrations imposed at the top of the boundary layer.

Finally, the normal fluxes of chloride and suppressor in the electrolyte adjacent to the deposit surface and the rates of their adsorption are equated to yield

$$-\left(z_{Cl}u_{m,Cl}FC_{Cl}\nabla\phi + D_{Cl}\nabla C_{Cl}\right)\cdot\hat{n} = \Gamma_{Cl}k_{Cl}^{+}C_{Cl}(1-\theta_{Cl}) \quad [17]$$

and

$$-D_P\nabla C_P\cdot\hat{n} = \Gamma_P k_P^{+}C_P(\theta_{Cl}-\theta_P) \quad [18]$$

for saturation coverages Γ_i estimated as detailed earlier. As stated previously, the $(\theta_{Cl} - \theta_P)$ term captures the requirement that the suppressor only adsorbs on chloride. The rate at which each adsorbate is deactivated (e.g., through incorporation in the deposit) is given by the product of ν, θ_i and k_i^- through Eqs. 1 and 2.

The full system of equations was solved numerically using a finite element method employing the COMSOL Multiphysics software package. Selective mesh refinement in the regions of highest gradient (i.e., within the TSV and boundary layer) was used to reduce computational burden while improving model accuracy. TSV deposition profiles were obtained using triangular mesh nodes of 1 μm on a side in the refined regions, containing approximately 2000 total mesh elements, and the overall charge balance error (the fractional difference between the total integrated currents at the counter electrode and the substrate) was less than 0.1%. All simulations were performed on a Dell Optiplex 980 desktop computer with an Intel Core i5 CPU@ 3.20 GHz and 8 GB RAM using a Windows 7 Enterprise 64-bit operating system. FEM simulations coupled the following COMSOL version 5.3 modules: secondary current distribution, transport of dilute species, separate coefficient form boundary partial differential equation for both chloride and suppressor, and deformed geometry. A moving boundary smoothing parameter of 1, geometry shape order of 2 and hyperelastic mesh smoothing type were used in the deformed geometry module (see COMSOL documentation for detailed explanation on how these conditions impact moving boundary convergence). Simulations took on the order of tens of minutes. In certain instances, periodic remeshing was performed to help computations proceed further in time. However, in contrast to the level set approach used previously,[5] the front tracking simulation code cannot conveniently continue beyond impingement of growing surfaces that marks the

NIST Author Manuscript NIST Author Manuscript NIST Author Manuscript

inception of seam or void formation. Maps of chloride incorporation were compiled in COMSOL using line plots of $\Gamma_{Cl} k_{Cl}^{-} \theta_{Cl}$ where the line thickness is equivalent to the integrated velocity (i.e., displacement) over each 10 second time interval.

Deposition and Simulations on Patterned Substrates

A direct comparison between experimental Cu deposition in TSVs (upper row) and deposition simulations (lower row) is shown in Figure 5. Experimental conditions are focused on applied potentials that lie positive of the onset of suppression breakdown observed in the slow scan voltammograms in Figure 1a. Accordingly, the free surface surrounding the vias is in a passive state while active Cu deposition occurs within. Copper deposits on all surface segments below the passive-active transition, with the location of the sidewall transition being a function of Cl^- concentration and potential. For 20 µmol/L Cl^-, active Cu deposition is nearly conformal at the most positive potentials, becoming less so at more negative potentials. For the most negative potential examined, corresponding to the voltammetric threshold of suppression breakdown, Cu deposition erupts from the via and grows onto the surrounding field. For 40 µmol/L Cl^- the Cu deposition exhibits a similar shape evolution but with the passive-active transition at a given potential shifted to greater depth within the via. For 80 µmol/L Cl^- the trend continues, with deposition shifted even further toward the bottom of the via for all but the most negative potential. Examination reveals an important dependence on potential with a shift from passive-active sidewall bifurcation to bottom-up filling at more positive values, i.e., −0.54 V. For all three Cl^- concentrations passivation of the entire via surface occurs at the most positive potential(s), the visible deposits having formed at early times, prior to complete passivation.

The simulations are qualitatively consistent with the experimental observations concerning the onset of metal deposition, capturing both the significant downward shift in the location of passive-active transition with increasing Cl^- concentration and the progressive upward shift with decreasing potential. At the most positive potentials the model predicts complete passivation after a brief period of deposition at −0.46 V with 40 µmol/L Cl^-, the same occurring at a longer time in the case of 20 µmol/L as well as 80 µmol/L Cl^- (not shown), as observed experimentally. The model is less accurate in capturing behavior at the most negative potentials where Cu deposition shifts to the top of the TSV and grows onto the field. The simulations reveal the change but with a −20 mV to −60 mV shift compared to experiment. Likewise, the model does not completely capture the detailed shape change as deposition shifts to bottom-up filling in the 80 µmol/L Cl^- experiment at −0.54 V.

The corresponding simulations of Cl^- coverage along the outer wall of the annular TSV are shown for the halide concentrations and applied potentials in Figures 6a–6c. For all three halide concentrations the passive-active transition zone shifts upward toward the via mouth as the overpotential is decreased in 20 mV increments. The magnitude of the shift with each increment is much smaller at the intermediate potentials, consistent with the modest displacements of the passive-active transition zone in the experimental results in Figure 5. The larger shift of the transition zone position at more negative potentials, particularly for 40 µmol/L and 80 µmol/L Cl^-, roughly captures the discontinuous shift of Cu deposition out of the TSV and onto the field observed experimentally. For a given potential, the transition

NIST Author Manuscript NIST Author Manuscript NIST Author Manuscript

region shifts deeper into the via as the Cl^- concentration is increased, with the coverage at the most positive potentials, i.e. –0.46 V at 80 μmol/L, approaching a saturated chloride coverage even at the via bottom.

The suppression breakdown transition can be parameterized by the depth within the TSV where metal deposition is at its maximum. The location of the passive-active transition measured from the optical micrographs, Figure 5, corresponds to either the thickest location in the deposit, or, for deposits with no obvious maximum, the highest location where the full thickness is achieved. Computational values are analogously defined as either the thickest location of the deposit in the simulation, or, for conditions that exhibit no local maximum, the height at which 90% of the maximum thickness is achieved. Comparison of the observed transition depths with simulations is summarized in Figure 7. As was evident qualitatively from Figure 5, the S-NDR model captures the shift to greater depths with increasing chloride concentration as well as the upward shift at more negative potentials observed in the intermediate potential range. The model also captures the seemingly discontinuous displacement up the via at the most negative potentials, although it does so at values 20 mV to 40 mV more negative than observed experimentally.

Temporal evolution during via filling at intermediate potentials is shown in Figure 8a. For deposition in electrolyte containing 20 μmol/L Cl^- at –0.52 V and 40 μmol/L Cl^- at –0.52 V as well as –0.54 V, the location of the passive-active transition remains fixed initially. After ten minutes the deposits on the sidewalls impinge, resulting in the formation of a void or seam due to metal ion depletion. For 20 μmol/L Cl^- at –0.52 V, growth subsequently shifts upward from the point of collision, filling the remaining portion of via in a void-free manner suggestive of bottom-up filling. For 40 μmol/L Cl^- at –0.52 V the uniform thickness of the active deposit indicates metal ion depletion is less severe. Sidewall impingement occurs lower in the via and leaves a steep v-notch growth front. During subsequent deposition the notch largely fills but with limited upward motion of the passive-active transition before the entire growth front stops moving by 30 minutes. At the more negative potential of –0.54 V, significant depletion yields a large void below the sidewall impingement point. As with the 20 μmol/L Cl^- at –0.52 V, the impingement is followed by a transition to more complete filling. However, smaller voids appear in the upper quarter of the via. Evidently, when the passive-active transition manifests in conformal, and eventually subconformal, sidewall deposition, void-free filling is not possible at a fixed applied potential for these dilute Cl^- electrolytes. An increase to 80 μmol/L Cl^- yields a shift to bottom-up growth early in the filling process. At –0.52 V, however, the bottom-up growth rate slows with time and eventually stops, leaving the via less than half-filled after 30 min. At –0.54 V the bottom-up growth dynamic flattens the initial v-notched growth front as it advances to fill three-quarters of the via height by 30 minutes. The average growth rate between 10 min and 30 min of ≈ 21 nm/s corresponds to a current density of ≈ –58 mA/cm^2. At –0.56 V the initial sidewall bifurcation occurs slightly higher in the via followed by a transition to bottom-up growth that leaves a narrow central void formed by sidewall collision within 5 min. This is followed by bottom-up propagation of the v-shaped growth front, which reaches the free surface in 20 minutes and then erupts onto the field. In this case filling proceeds at an average rate corresponding to a current density in excess of ≈ –120 mA/cm^2.

NIST Author Manuscript

NIST Author Manuscript

NIST Author Manuscript

Computational predictions of feature filling for the conditions in Figure 8a are shown in Figure 8b. Given that the simulations are only computed through impingement of the deposits on the sidewalls, good agreement between experiment and simulation is evident for 20 μmol/L Cl^- and 40 μmol/L Cl^-. Specifically, the location of the passive-active transition remains fixed through impingement and the voids predicted to form due to copper ion depletion vary in size consistent with experiment. For 80 μmol/L Cl^- filling begins with sidewall bifurcation near the bottom of the via and then evolves into one of three different morphologies depending on the applied potential. At –0.52 V, the simulations predict complete passivation with negligible deposition occurring after 10 minutes. This is at odds with the experiment where a transition to bottom-up growth occurs before deposition eventually ceases. At –0.54 V a transition from passive-active growth on the lower sidewall to bottom-up deposition occurs by 10 minutes. This is followed by bottom-up growth that fills half of the via by 20 minutes. The growth front forms a v-shaped cusp whose vertical span corresponds to the spatial extent of the Cl^- coverage transition shown in Figure 6c. The fill height is in good agreement with experiment although the v-shape cusped growth front is noticeably different from the near planar geometry observed in experiment. Interestingly, simulations predict that growth ceases shortly after 20 minutes, capturing the experimental behavior 20 mV more positive. At –0.56 V a higher position of the passive-active sidewall transition followed by rapid sidewall propagation yields impingement and void formation in the bottom-most section of the via in good agreement with experiment. Unfortunately, the limitations of the front tracking code prevented simulation beyond this point. The right-hand vias at 80 μmol/L Cl^- and –0.54 V show simulations using k_P^+ and k_P^- equal to 2500 $m^3/mol \cdot s$ and 1×10^7 1/m, respectively, instead of the values reported in Table I. These values are consistent with those used for bottom-up filling in higher Cl^- concentrations.[3,5] It is evident that the 50-fold increase in k_P^+ and 200-fold increase in k_P^- has negligible impact on the feature filling predictions; the values for k_P^+ and k_P^- (and, less so, their ratio) have significant latitude when fitting voltammetric data in Fig. 2, providing a range of values also capable of effectively capturing feature filling characteristics.

As suppression breakdown is linked to Cl^- consumption under these conditions, a selection of simulated Cl^- incorporation maps (right-hand vias) and Cl^- coverage contours (left-hand vias) are shown in Figure 9. They provide testable predictions of impurity composition and distribution that might be tied to the microstructure of the deposits, as was previously done for polymer incorporation in Ni filled TSV.[32] At 20 μmol/L Cl^- and –0.50 V the Cl^- incorporation is highest at the leading edge of the deposit, with comparatively little impurity toward the bottom of the Cu via. Chloride coverage contours show that upon sidewall impingement $\theta_{Cl} > 0.5$ above the void, suggesting possible passivation if the simulations could be continued through impingement. The simulation at 80 μmol/L Cl^- and –0.52 V shows similar behavior, with higher chloride incorporation at the leading edge of the deposit and $\theta_{Cl} = 1$ everywhere on the final coverage contour. As this condition does not result in void formation, continued simulation is possible and does predict complete suppression of deposition by 10 minutes, as seen in Fig. 8b.

At potentials more negative by 20 mV for both concentrations the regions of highest chloride incorporation shift from the leading edge of the deposit to the passive deposits along the side-walls of the via. Experiment shows that in 20 μmol/L Cl^- and –0.52 V the deposit

NIST Author Manuscript NIST Author Manuscript NIST Author Manuscript

continues to grow upward after void formation (Fig. 8a), whereas the –0.50 V condition passivates shortly after impingement (not shown). The final contour at –0.52 V shows $\theta_{Cl} < 0.5$ on the deposit above the point of impingement (excluding the side-wall), indicating upward growth would continue if the simulations could be carried past void formation. The simulation for 80 μmol/L Cl^- and –0.54 V passivates after about 20 minutes, evidenced by $\theta_{Cl} = 1$ everywhere on the final contour line. The highest levels of chloride incorporation are in the region of the active-passive transition during early deposition ($t < 8$ min) and along the side walls after transitioning to bottom-up deposition. The white lines for the 80 μmol/L Cl^- conditions are artifacts of plotting related to mesh size in the simulations and do not indicate formation of seams or voids (see Fig. 8b for simulated growth profiles).

The impact of transport on the location of the passive-active transition was examined by varying the rotation rate of the TSV patterned wafer fragment during Cu deposition at –0.50 V. As shown in Figure 10, experiments (left hand side) reveal a modest downward shift of the sidewall bifurcation within the via with an increase in rotation rate. Computational predictions in Figure 10 (right hand side), modeling the decreased hydrodynamic boundary layer thickness (δ) with rotation rate, mirror the slight downward shift with increased transport. For the wafer specimens' spindle rotation rates of 25 rpm and 1600 rpm, δ decreases from 50 μm to 6.25 μm, respectively. Accordingly, the location of the passive-active transition at 5 minutes of deposition is deeper by 6 μm for filling in 20 μmol/L Cl^- and 7 μm for filling in 40 μmol/L Cl. Isocontours of Cl^- electrolyte concentration in the left-hand side of the vias in the simulations show that the lowest contour lines (0.1% of bulk concentration) are at or below where the Cu deposition is thickest (i.e., has fully activated), revealing the Cl^- burial within the deposit in the transition zone and associated depletion of Cl^- in the electrolyte below it. Isocontours of metal ion concentration shown in the right-hand side of the vias in the simulations indicate that Cu^{2+} depletion is also significant even at –0.50 V, with the most severe depletion condition (20 μmol/L Cl^-, δ = 50 μm) yielding 29% of the bulk cupric concentration at the via bottom.

The above findings demonstrate that in contrast to electrolytes containing higher Cl^- concentration, complete bottom-up filling of the TSV in low Cl^- electrolytes is difficult due to either void formation from sidewall impingement or quenching of the transient bottom-up growth dynamic at the lower overpotentials. In previous work with PEI suppressed Ni, Co and Au deposition[32–36] that exhibit analogous sidewall passive-active behavior, potential waveforms were used to progressively advance the location of suppression breakdown upwards in the feature to enable complete TSV filling. In a related vein, galvanodynamic waveforms have been used to optimize the time required for bottom-up Cu deposition in TSV.[37] Accordingly, the use of potential waveforms to drive complete filling of TSV in dilute Cl^- electrolytes was examined computationally. The resulting growth contours for the three different Cl^- containing electrolytes are shown in Figure 11. The potential step waveforms are designed to develop a v-notched growth front to counteract the depletion effects that otherwise lead to subconformal growth, reentrant sidewalls and void formation. Starting deposition at a small overpotential ensures the passive-active transition is located deep within the vias. The applied potential is then advanced in 20 mV to 60 mV increments every 5 to 10 minutes depending on the chloride concentration. The left-hand side of the annular vias in Figure 11 shows filling contours at 5 min intervals while the right-hand side

NIST Author Manuscript NIST Author Manuscript NIST Author Manuscript

depicts the fully filled volume. For the low Cl^- electrolytes, 20 μmol/L and 40 μmol/L, many steps are required to incrementally shift the passive-active transition upwards in a manner that effectively couples the shift in position of the Cl^- coverage depletion profile (Figure 6) with the deposition rate to define and maintain the desired v-notch shape required for void-free filling.

At a higher Cl^- concentration, 80 μmol/L, a transition from sidewall passive-active bifurcation to bottom-up behavior was both observed and predicted during potentiostatic TSV filling at −0.54 V (Fig. 8). However, computations indicate that the process stops after 20 minutes. By implementing a three step potential waveform to shift the passive-active transition upward, void-free filling of the annular TSV is predicted to be accomplished in 28 minutes. Higher concentrations of chloride allow for more negative potentials to be used during TSV filling, resulting in shorter times to achieve fully filled vias.

Discussion

The link between the formation and breakdown of the polyether-halide suppressor layer and selective filling of recessed surface features such as TSV has been examined with constraints imposed on the adsorption, and co-adsorption, of the respective additives. For dilute Cl^- concentrations the formation and stability of the suppressor layer is limited by the available halide flux that, convolved with surface topography and the kinetics of metal deposition, impacts TSV filling. This complements recent experimental work focused on the effects of dilute poloxamine suppressor on TSV filling in the presence of a higher Cl^- concentration.[6] In both cases positive feedback arises from disruption of the suppressor surface phase by metal deposition as evidenced by hysteretic S-shaped NDR voltammetry. Bifurcation and emergence of a two-state, active–passive surface with voltammetric cycling reflects the mismatch between slow material transport and the more rapid electrical response of the system. On non-planar surfaces such as metallized TSV, active deposition develops preferentially on recessed surfaces. In the present work the negative-going voltammetric threshold for suppression breakdown is used to parameterize the kinetics of disruption and consumption of the halide layer, and the derived kinetics are subsequently used for simulation of feature filling. For selective deposition in the recessed TSV the applied potential is required to be more positive than that associated with the voltammetric threshold for suppression breakdown measured voltammetrically (i.e., on the RDE surface). Common to both voltammetry and the feature filling program is a period during which the additives interact with the respective workpiece at small overpotentials before the potential is advanced to more negative values for feature filling. For feature filling in 20 μmol/L to 40 μmol/L Cl^- and 100 rpm the idle time of 120 s at −0.4 V is similar to the 90 s to 100 s required for the voltammetric scan to reach the suppression breakdown potential. A difference between these experiments is the workpiece geometry and corresponding hydrodynamic flow fields, RDE versus shear plane, where transport to the via-patterned wafer fragments is expected to be slightly enhanced.

Voltammetric analysis of the potential dependence of the suppression breakdown under vigorous convection, i.e. 1600 rpm, reveals the threshold shifts ≈ −60 mV/log[Cl^-] consistent with an adsorption isotherm for a $1e^-$ halide electrosorption reaction.

$$Cu + Cl^{-}_{aq} = CuCl_{ads} + e^{-} \quad [19]$$

Detailed description of the breakdown process with regard to the coverage and surface structure evolution of the halide layer in the presence of metal deposition remains to be fully developed although a variety of STM, SXRD and SERIAS studies provide some hints of applicable phenomena and dynamics.[28,31,45–48] Looking to the future, more accurate models will need to address the potential dependent kinetic rate constants congruent with the additive isotherms. In the present work poloxamine adsorption is stipulated, in Eq. 2, to not exceed the Cl^- coverage, thereby capturing the sequential co-adsorption of the polyether suppressors on Cl^- known to occur in this system. For the dilute Cl^- concentrations examined herein, the corresponding flux and co-adsorption of 40 μmol/L Tetronic 701 polyether is rapid enough that formation of the Cl^- - Tetronic 701 suppressor phase is essentially determined by the transport limited kinetics of halide adsorption. A brief sensitivity analysis revealed significant latitude in the k_P^+ and k_p^- values (and less so the k_P^+ / k_P^- ratio) that can be used without significantly impacting the fitting of voltammetry (Fig. 2) or feature filling in the dilute Cl^- electrolytes (i.e., 80 μmol/L Cl^- and −0.54 V condition in Fig. 8b). In contrast, for the lower Cl^- concentrations and RDE rotation rates significant deviation from the Cl^- adsorption isotherm is evident due to insufficient flux required to form a fully developed suppressor layer. Upon increasing the concentration to 20 μmol/L Cl^-, a fully formed halide adlayer is obtained on the RDE at 100 rpm with an equivalent coverage expected on the field region of the TSV patterned specimens. The longer transport path and additional surface area of the recessed annular vias will delay the formation of a saturated Cl^- coverage. The resulting lag in co-adsorption of the polyether and development of suppression is such that metal deposition initiates in the more remote sections of the TSV. Simulation of the sidewall Cl^- coverage after 2 min of deposition in the TSV (Fig. 6) captures the situation as a function of potential and Cl^- concentration.

Similar shape transitions associated with suppression breakdown on TSV sidewalls have been reported for Au, Co and Ni electroplating in the presence of a single polymer suppressor.[32–36] The flux balance between transport-limited suppressor adsorption and its consumption by metal deposition fix the position of the passive-active transition as a function of additive concentration, hydrodynamics and potential. For the Au, Co and Ni systems metal ion depletion is less significant compared to that for the dilute suppressor additive in this Cu study and, thus, maintaining the conditions for conformal deposition below the passive-active transition is easily realized. In contrast, more significant metal ion depletion accompanies the suppressor gradients during Cu deposition under the present conditions as well as during bottom-up filling in more concentrated Cl^- electrolytes.[1,3,5,6] The shift in the position of the passive-active transition in the Cu system with hydrodynamics is weaker than was observed for Ni, Co or Au deposition. The modest impact (Fig. 10) is congruent with the decreased dependence of the voltammetric breakdown potential on halide transport for concentrations greater than 20 μmol/L Cl^- (Fig. 2). These observations reflect the shift from transport limited Cl^- coverage to behavior influenced more by the corresponding isotherm.

NIST Author Manuscript NIST Author Manuscript NIST Author Manuscript

NIST Author Manuscript NIST Author Manuscript NIST Author Manuscript

For dilute Cl^- concentrations, the location of the passive-active transition shifts deeper into the TSV as the Cl^- concentration increases from 20 μmol/L to 80 μmol/L. At 80 μmol/L Cl^- deposition initiates with sidewall breakdown near the bottom of the via and the growth front shifts to bottom-up filling similar to that reported for higher Cl^- concentration.[1,6] That said, void-free changeover between the two growth modes, as well as sustained upward propagation of the bottom-growth front, is a sensitive function of the applied potential. For the 80 μmol/L experiments shown in Fig. 8 the transition to void-free bottom-up growth is underway at −0.54 V. However, the processing window is narrow: the bottom-up growth front stalls at −0.52 V and voids associated with the transition point between sidewall deposition and bottom-up growth are evident at −0.56 V. In any case, for the given TSV features, 80 μmol/L Cl^- corresponds to the threshold halide concentration where the system pivots between the two different filling modes.

The opposite limit, where filling behavior is controlled by a dilute suppressor concentration, was examined previously. Feature filling also exhibits a transition from sidewall breakdown to bottom-up filling. However, in that case, the details of the transition were intimately associated the initial conditions.[6] Critical to both sidewall breakdown and bottom-up filling in the S-NDR mechanism is a depletion gradient of suppressor or chloride within the via.[1,5,32–36] In these studies, desorption of the adsorbates is assumed to occur by deactivation (the adsorbate desorbs into solution but cannot readily re-adsorb on the interface) or incorporation into the growing deposit. Computations of polymer incorporation in nickel TSV were previously correlated to electron backscatter diffraction (EBSD) measurements, indicating higher levels of predicted impurity in the regions of high grain refinement.[32] Incorporation maps in Fig. 9 similarly predict chloride concentration within the copper deposits. Several studies have shown copper morphology is influenced by the solution additive chemistry and plating parameters, with incorporation of impurities leading to challenges with adhesion and voiding of copper-solder contacts.[48–51] As a result, several attempts to measure impurity incorporation in copper have been made using techniques including: energy dispersive spectrometry (EDS),[50,51] time-of-flight secondary ion mass spectrometry (TOF-SIMS),[52] combined laser ablation and ion mass spectrometry[53,54] and dynamic secondary ion mass mass spectrometry (DSIMS).[55] These methods have demonstrated qualitative trends for which additives (chloride, suppressor, accelerator or leveler) most influence impurity incorporation during copper deposition. For Cl^- incorporation, however, quantitative values for similar electrolyte compositions (i.e. PEG-Cl) range across several orders of magnitude, from 6 to 700 ppm by mass. Computations of chloride incorporation in Figure 9 show the highest concentration levels equal to ≈ 240 mol/m^3 (or 960 ppm Cl^- by mass), in nominal agreement with the high end of previously reported values in literature. That said, the regions with high Cl^- incorporation are highly localized compared to the overall volume of material assayed by the above methods and an accurate comparison requires a careful assessment of this difference. Indeed the incorporation maps point to strong spatial variations that includes preferential incorporation of the Cl^- along the sidewall that is similar to recent scanning Auger microscopy that show the majority of C impurities are preferentially localized to feature sidewalls.[53]

In dilute Cl^- solutions where sidewall breakdown is dominant, significant metal ion depletion below the passive-active transition makes void or seam-free TSV filling with a

NIST Author Manuscript NIST Author Manuscript NIST Author Manuscript

fixed applied potential difficult to impossible. However, adopting the strategy previously used for Ni, Co and Au deposition,[32–36] a potential waveform might be used to advance the location of the passive-active breakdown upwards while maintaining a v-notch growth profile that balances the surface gradient in Cl^- and polyether coverage against that of metal ion depletion. When optimized the prospect for void-free or seam-free filling of the TSV might be enabled using this approach.

In contrast to passive-active transition zone mediated TSV filling, the bottom-up growth is intrinsically capable of void-free filling. That said, bottom-up filling in 80 μmol/L Cl^- is very sensitive to the processing conditions. More robust bottom-up filling with a slightly convex growth front has been previously demonstrated when the Cl^- concentration is 10 times greater, i.e. 1 mmol/L.[1,6] The kinetic rate constants k_P^+ and k_P^- for the polymers adsorption and disruption become much more important for effective simulation of the growth mode under these conditions.[3,5] For example, the lower range of possible k_P^+ and k_P^- values listed in Table I, while suitable for describing the low Cl^- experiments that are dominated by Cl^- adsorption, are inadequate for capturing bottom-up filling (not shown); rather complete passivation of the TSV is predicted for the experimentally relevant applied potentials in 1 mmol/L Cl^- and 25 μmol/L poloxamine. This is consistent with prior simulations demonstrating that higher k_P^+ and k_P^- values yield bottom-up TSV filling where the adsorbed polymer is removed from the interface at a rate proportional to the local growth velocity.[3,5] Several different mechanisms that might account for such disruption can be envisioned but in all cases it is the interaction between metal deposition and Cl^--polyether suppressor breakdown that provides the positive feedback that underlies filling process. Continued research is necessary to more fully understand the nature of the bottom-up growth process from its sensitivity to processing conditions and history, to the chemical nature of moving surfaces and additive adsorption thereupon and the collective impact of these processes on microstructure.

Conclusions

Cu deposition in TSV depends on the formation and disruption of the suppressor phase formed by co-adsorption of polyether and halide. The effect of limiting the available halide on voltammetric behavior and feature filling was examined. For suitably high transport conditions the voltammetric onset of metal deposition on a Cu RDE follows a −60 mV/log[Cl^-] dependence indicating suppression breakdown is associated with a change in the coverage and/or structure related to the halide adsorption isotherm. TSV filling was performed at potentials positive of the voltammetric onset, the difference reflecting the additional transport constraint associated with forming the suppressor phase on surfaces within the recessed geometry. Two different growth morphologies were observed during TSV filling. For Cl^- concentration   80 μmol/L active deposition initiates with suppressor breakdown on the via sidewalls with the location being a function of Cl^- concentration, hydrodynamics and potential. The necessity of halide adsorption as a precursor to polyether adsorption accounts for the shift of the location of the passive-active transition with Cl^- concentration. Simulations of the breakdown process are quantitatively modeled as a balance between halide flux to form the suppressor layer versus its disruption by metal deposition and halide incorporation in the growing deposit. For 20 μmol/L and 40 μmol/L Cl^- in

NIST Author Manuscript NIST Author Manuscript NIST Author Manuscript

particular, at the appropriate potentials deposition occurs below the passive-active transition point and, depending on the extent of metal ion depletion, results in void or seam formation when the sidewalls impinge. For 80 μmol/L Cl^-, the location of suppression breakdown is placed close to the TSV bottom and shortly thereafter a shift to bottom-up deposition occurs. Depending sensitively on potential, the original v-notch growth front flattens as the bottom surface moves upwards; however, in certain cases growth stalls. This is in contrast to higher Cl^- concentrations where complete void-free TSV filling can be reliably obtained in 15 to 20 minutes. Accordingly, filling with 80 μmol/L Cl^- represents a transition in behavior from that controlled by halide adsorption and disruption to one controlled by polymer adsorption dynamics. Predictive modeling of the latter will be detailed in a subsequent publication.

Spatial predictions of chloride incorporation indicate higher impurity levels in the region of the passive-active transition and along the sidewalls in the case of bottom-up feature filling. Additional efforts to measure chloride levels in electrodeposited Cu TSV or to correlate impurity predictions with deposit morphology by EBSD are needed to evaluate the accuracy of the S-NDR model presented here. Finally, an alternative approach to complete feature filling in the dilute chloride electrolyte was described. It involves the use of potential waveforms to progressively advance the location of passive-active sidewall upwards while controlling the dimension of the v-notch to minimize void or seam formation. The strategy is analogous to that previously demonstrated for Ni, Co and Au deposition in the present of single dilute inhibitor.

Acknowledgments

Identification of commercial products in this paper is done to specify the experimental procedure. In no case does this imply endorsement or recommendation by the National Institute of Standards and Technology. The copper seeded, annular TSVs were kindly provided by D. Edelstein of IBM.

References

1. Moffat TP and Josell D, J. Electrochem. Soc, 159, D208 (2012).
2. Wu HLH and Lee SWR, 2012 4th Electronic System-Integration Technology Conference, Amsterdam, Netherlands, pp. 1, 2012.
3. Josell D and Moffat TP, J. Electrochem. Soc, 159, D570 (2012).
4. Yang L, Radisic A, Deconinck J, and Vereecken PM, J. Electrochem. Soc, 160, D3051 (2013).
5. Wheeler D, Moffat TP, and Josell D, J. Electrochem. Soc, 160, D3260 (2013).
6. Josell D and Moffat TP, J. Electrochem. Soc, 165, D23 (2018).
7. Menk LA, Baca E, Josell D, P Moffat T, Blain M, Smith A, Dominguez J, McClain J, Yeh PD, and Hollowell AE, J. Electrochem. Soc, 166(1) D3066 (2019).
8. Hayase M, Taketani M, Hatsuzawa T, and Hayabusa K, Electrochem. & Solid State Lett, 6, C92 (2003).
9. Hill MRH and Rogers GT, J. Electroanal. Chem, 86, 179 (1978).
10. Yokoi M, Konishi S, and Hayashi T, Denki Kagaku, 51, 460 (1983).
11. Yokoi M, Konishi S, and Hayashi T, Denki Kagaku, 52, 218 (1984).
12. Healy JP, Pletcher D, and Goodenough M, J. Electroanal. Chem, 338, 155 (1992).
13. Nagy Z, Blaudeau JP, Hung NC, Curtiss LC, and Zurawski DJ, J. Electrochem. Soc, 142, L87 (1995).
14. Kelly JJ and West AC, J. Electrochem. Soc, 145, 3472 (1998).
15. Doblhofer K, Wasle S, Soares DM, Weil KG, and Ertl G, J. Electrochem. Soc, 150, C657 (2003).

NIST Author Manuscript
NIST Author Manuscript
NIST Author Manuscript

16. Hebert KR, J. Electrochem. Soc, 152, C283 (2005).
17. Hebert KR, Adhikari S, and Houser JE, J. Electrochem. Soc, 152, C324 (2005).
18. Walker ML, Richter LJ, and Moffat TP, J. Electrochem. Soc, 152, C403 (2005).
19. Dow W-P, Yen M-Y, Lin W-B, and Ho S-W, J. Electrochem. Soc, 152, C769 (2005).
20. Willey MJ andWest AC, J. Electrochem. Soc, 153, C728 (2006).
21. Huerta Garrido ME and Pritzker MD, J. Electrochem. Soc, 156, D36 (2009).
22. Willey MJ and McInerney EJ, J. Electrochem. Soc, 156, D98 (2009).
23. Huerta Garrido ME and Pritzker MD, J. Electrochem. Soc, 156, D175 (2009).
24. Yang L, Radisic A, Deconinck J, and Vereecken PM, J. Electrochem. Soc, 161, D269 (2014).
25. Yang H, Dianat A, Bobeth M, and Cuniberti G, J. Electrochem. Soc, 164, D196 (2017).
26. Yang H, Krause R, Scheunert C, Liske R, Uhlig B, Preusse A, Dianat A, Bobeth M, and Cuniberti G, J. Electrochem. Soc, 165, D13 (2018).
27. Feng ZV, Li X, and Gewirth AA, J. Phys. Chem. B, 107, 9415 (2003).
28. Liu G-K, Zou S, Josell D, Richter LJ, and Moffat TP, J. Phys. Chem. C,122, 21933 (2018).
29. Krischer K, Mazouz N, and Flatgen G, J. Phys. Chem. B, 104, 7545 (2000).
30. Krischer K, Electroanal Chem J., 501, 1 (2001).
31. Moffat TP, Electrochemical Processing in ULSI Fabrication and Semiconductor/Metal Deposition II, The Electrochemical Society Proceedings, Vol 99–9, 41 (1999).
32. Braun TM, Kim S-H, Lee H-J, Moffat TP, and Josell D, J. Electrochem. Soc, 165, D291 (2018).
33. Josell D and Moffat TP, J. Electrochem. Soc, 163, D322 (2016).
34. Josell D, Silva M, and Moffat TP, J. Electrochem. Soc, 163, D809 (2016).
35. Josell D and Moffat TP, J. Electrochem. Soc, 164, D327 (2017). [PubMed: 28729743]
36. Josell D and Moffat TP, J. Electrochem. Soc, 160, D3035 (2013).
37. Yang L, Radisic A, Deconinck J, and Vereecken P, J. Electrochem. Soc, 162, D599 (2015).
38. Quickenden TI and Xu Q, J. Electrochem. Soc, 143, 1248 (1996).
39. Newman JS, Electrochemical Systems, Wiley, Hoboken, NJ (2004).
40. Gonzalez-Lopez J, Alvarez-Lorenzo C, Taboada P, Sosnik A, Sandez-Macho I, and Concheiro A, Langmuir, 24, 10688 (2008). [PubMed: 18785722]
41. Waggoner RA, Blum FD, and Lang JC, Macromolecules, 28, 2658 (1995).
42. Masaro L, Zhu XX, and Macdonald PM, Macromolecules, 31, 3880 (1998).
43. Shimada K, Kato H, Saito T, Matsuyama S, and Kinugasa S, J. Chem. Phys, 122, 244914 (2005). [PubMed: 16035823]
44. Dong J, Armstrong J, Chowdhry BZ, and Leharne SA, Thermochimica Acta, 417, 201 (2004).
45. Magnussen OM, Chem. Rev, 102, 679 (2002). [PubMed: 11890754]
46. Grunder Y, Stettner J, and Magnussen OM, J. Electrochem. Soc, 166, D3049 (2019).
47. Stuhlmann C, Wohlmann B, Park Z, Kruft M, Broekmann P, and Wandelt K, Solid-Liquid Interfaces, Macroscopic Phenomena-Microscopic Understanding, Topics in Applied Physics, Springer, New York., 85, 199 (2003).
48. Liu Y, Wang J, Yin L, Kondos P, Parks C, Borgesen P, Henderson DW, Cotts EJ, and Dimitrov N, J. Appl. Electrochem, 38, 1695 (2008).
49. Liu Y, Liang Y, Bliznakov S, Kondos P, Borgesen P, Henderson DW, Parks C, Wang J, Cotts E, and Dimitrov N, IEEE. T. Compon. Pack. T, 33, 127 (2010).
50. Yu T-Y, Lee H, Hsu H-L, Dow W-P, Cheng H-K, Liu K-C, and Chen C-M, J. Electrochem. Soc, 163, D734 (2016).
51. Lee H, Yu T-Y, Chen H-K, Liu K-C, Chan P-F, Dow W-P, and Chen C-M, J. Electrochem. Soc, 164, D457 (2017).
52. Mroczka R, Lopucki R, and Zukocinski G, Appl. Surf. Sci, 463, 412 (2019).
53. Grimaudo V, Moreno-Garcia P, Cedeño Lopez A, Riedo A, Wiesendanger R, Tulej M, Gruber C, Lortscher E, Wurz P, and Broekmann P, Anal. Chem, 90, 5179 (2018). [PubMed: 29578694]

NIST Author Manuscript

NIST Author Manuscript

NIST Author Manuscript

54. Riedo A, Grimaudo V, Moreno-Garcia P, Neuland MB, Tulej M, Wurz P, and Broekmann P, J. Anal. At. Spectrom, 30, 2371 (2015).
55. Schmidt R, Beck T, Rooney R, and Gewirth A, IEEE 68th Electronic Components and Technology Conference, 1220 (2018).

NIST Author Manuscript

NIST Author Manuscript

NIST Author Manuscript

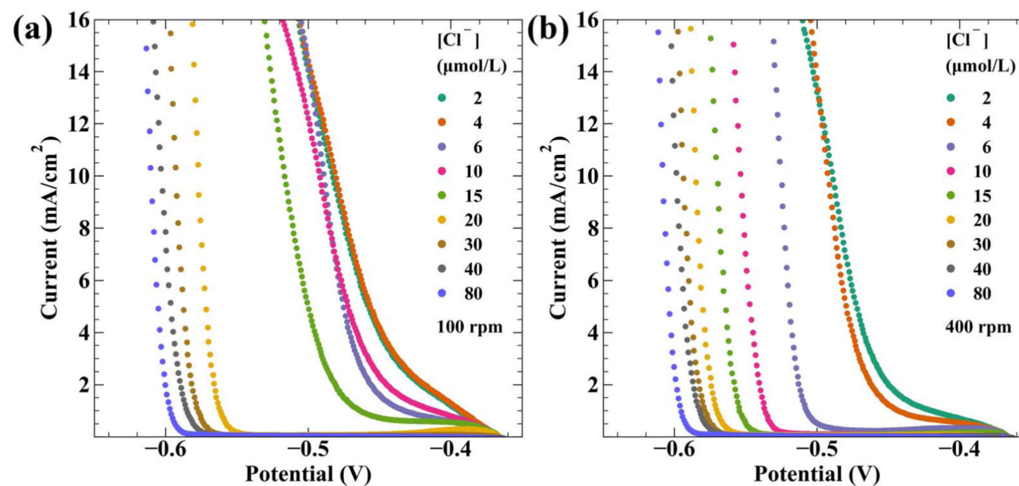

Figure 1.

Linear sweep voltammetry for Cu deposition at 2 mV/s in 1 mol/L $CuSO_4$–0.5 mol/L H_2SO_4 electrolyte containing 40 μmol/L Tetronic 701 with RDE rotation rate a) 100 rpm and b) 400 rpm in electrolytes containing the indicated chloride concentrations. Experimental currents are converted to current densities using the 0.20 cm^2 RDE area and were collected with 70% compensation for iR potential drop across the measured cell resistance (R ≈ 6.5 Ω). The current density is plotted against the applied potential vs. Hg/$HgSO_4$/saturated K_2SO_4.

NIST Author Manuscript

NIST Author Manuscript

NIST Author Manuscript

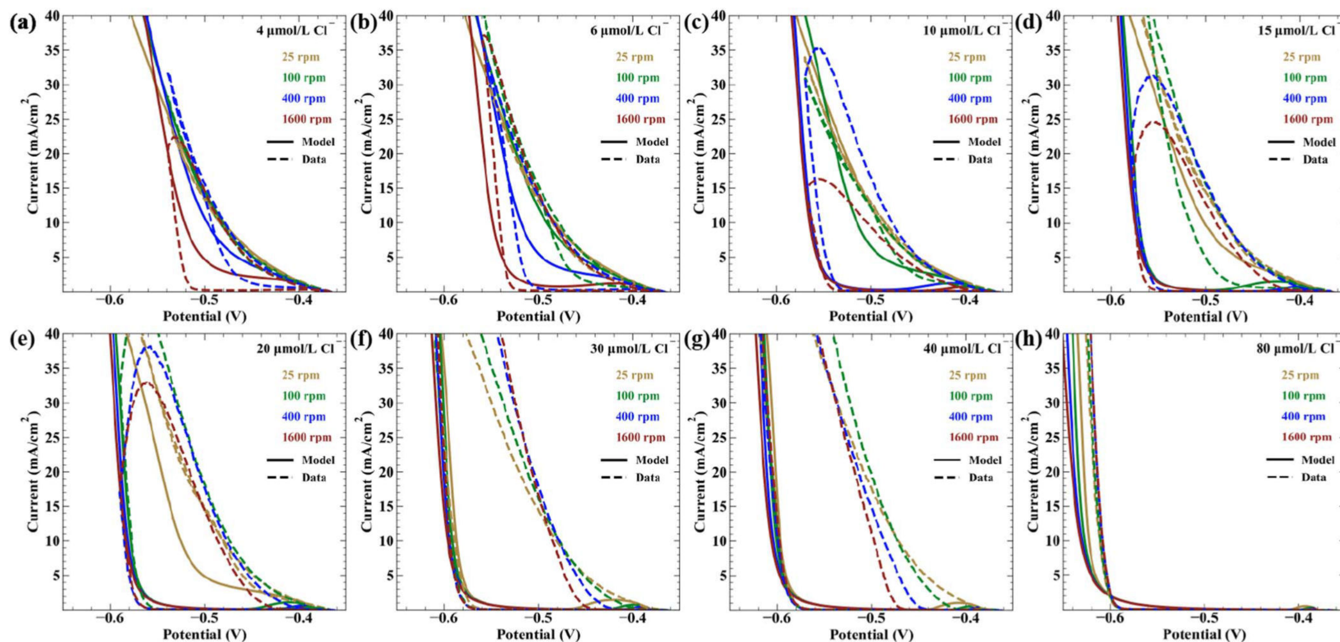

Figure 2.

Voltammetry at 2 mV/s for Cu deposition and S-NDR model in electrolytes with additive concentrations of 40 µmol/L Tetronic 701 and a) 4 µmol/L, b) 6 µmol/L, c) 10 µmol/L, d) 15 µmol/L, e) 20 µmol/L, f) 30 µmol/L, g) 40 µmol/L and h) 80 µmol/L Cl^- at the indicated RDE rotation rates. Only linear sweep voltammetry was performed for 80 µmol/L Cl^-; cyclic voltammetry is shown for all other conditions. Experimental currents are converted to current densities using the 0.20 cm^2 RDE area. The data, plotted against the applied potential, was collected with 70% compensation for iR potential drop across the measured cell resistance $R \approx 6.5\ \Omega$. The simulations account for potential drop due to the uncompensated portion of the cell resistance.

NIST Author Manuscript

NIST Author Manuscript

NIST Author Manuscript

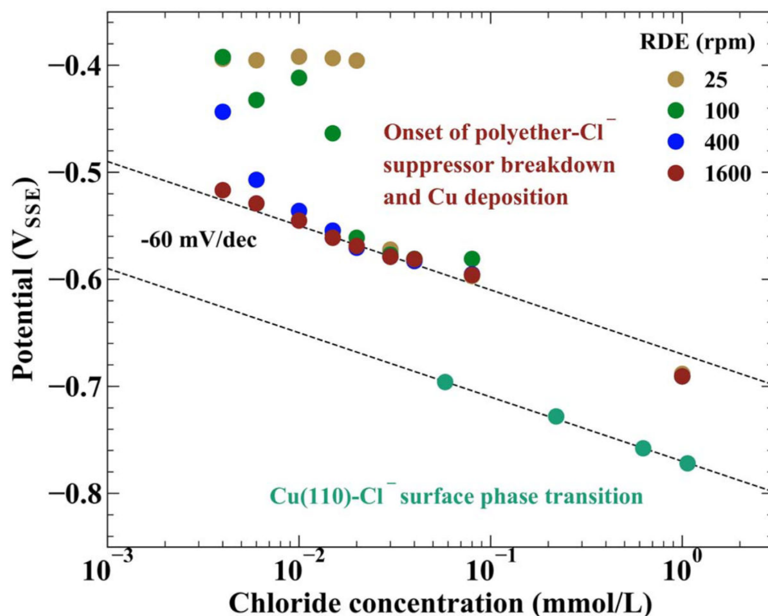

Figure 3.

The potential threshold for co-adsorbed halide-polyether suppressor breakdown during the first negative going voltammetric scan shown in Figure 2 as sampled at 1 mA/cm^2. For the highest RDE rotation rate, 1600 rpm (●), the threshold shifts −60 mV/dec congruent with breakdown occurring at a fixed Cl^- coverage. For slower rotation rates the breakdown potential is limited by the available halide flux and deviates from the isotherm at 10 μmol/L Cl^- for 400 rpm (●), 20 μmol/L Cl^- for 100 rpm (●) and 30 μmol/L Cl^- for 25 rpm (●). The values at 1 mmol/L Cl^- correspond to 25 μmol/L Tetronic 701.[6] Voltammetric examination of Cl^- adsorption on Cu(110) in x mmol/L KCl + 0.01 mol/L HClO4 at 20 mV/s reveals a phase transition with a peak potential (●) that shifts approximately −60 mV/dec.[31]

NIST Author Manuscript

NIST Author Manuscript

NIST Author Manuscript

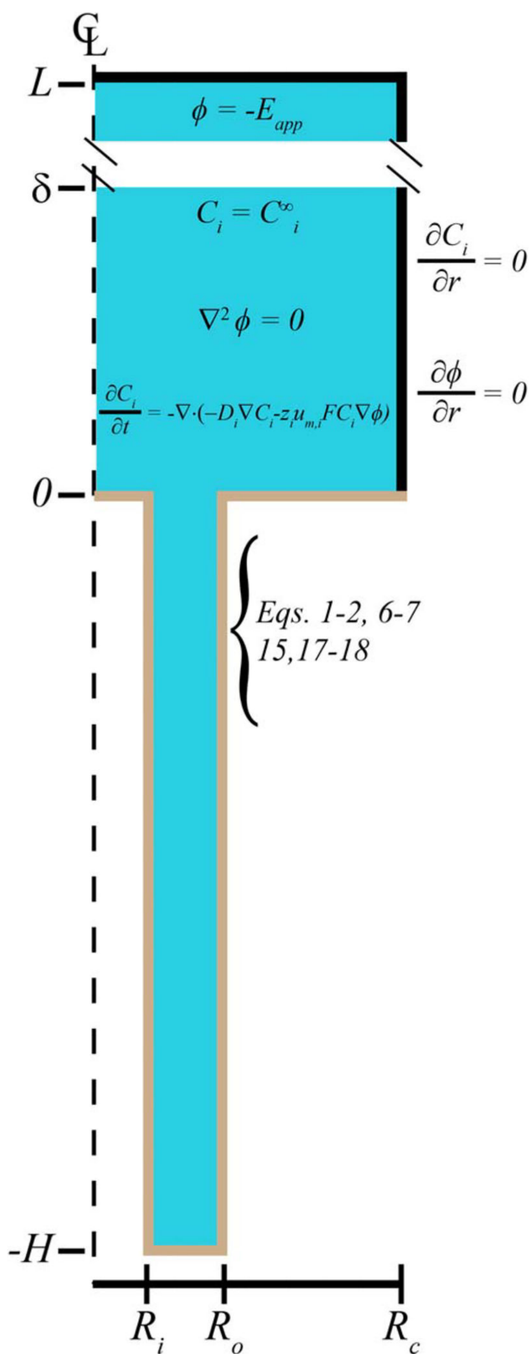

Figure 4.

Schematic of axisymmetric geometry used in the S-NDR model to simulate deposition in the annular TSV. Diffusion and electromigration are accounted for in the boundary layer. The subscript *i* indicates the species ($i = Cu^{2+}$, Cl^-, Tetronic 701, SO_4^{2-}, H^+, and Na^+) for the time and position dependent concentration fields. Potential distribution is computed relative to the counter/reference electrode located at *L*. Boundary conditions and surface reactions are specified or referenced to the relevant equations.

NIST Author Manuscript
NIST Author Manuscript
NIST Author Manuscript

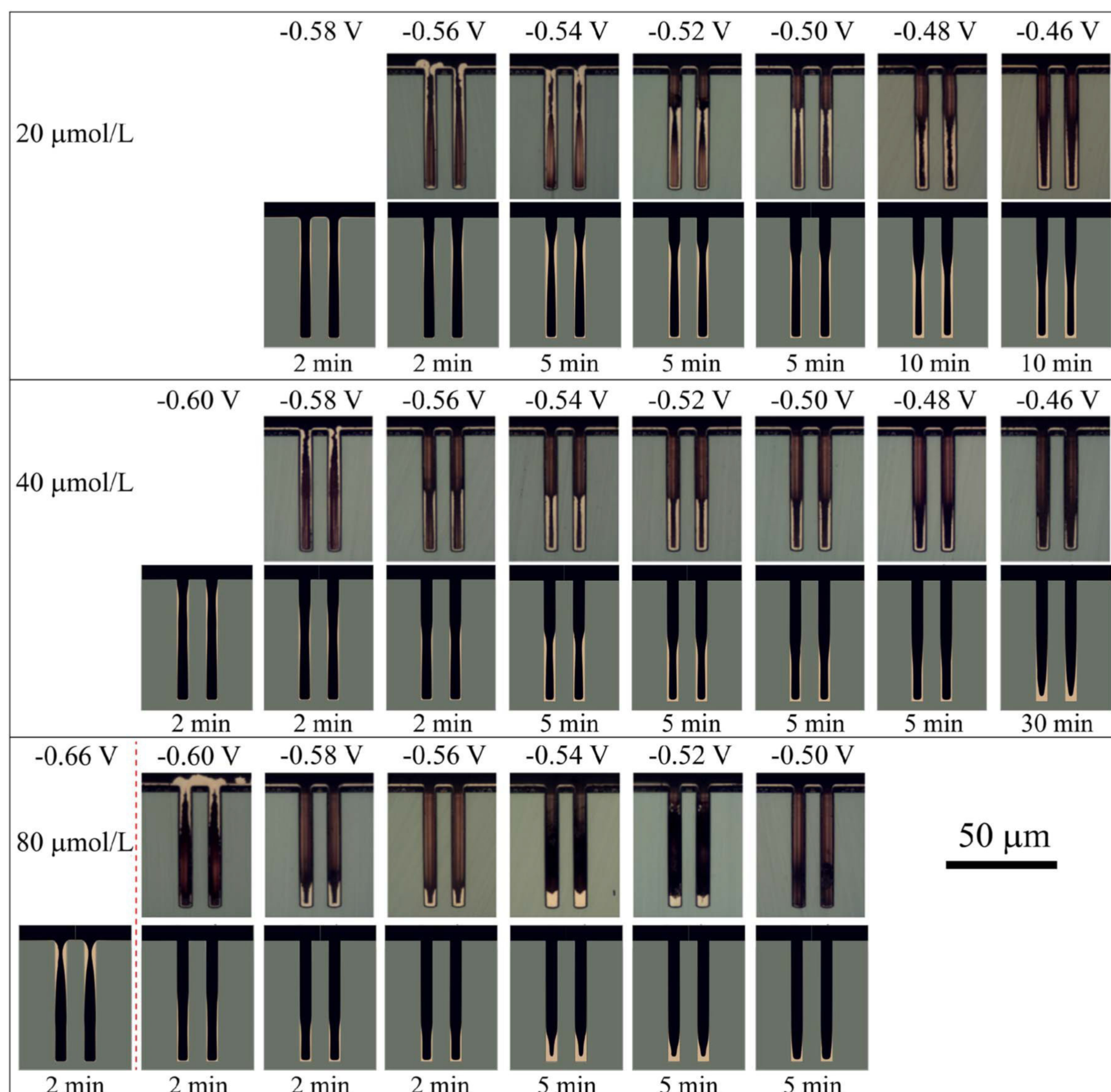

Figure 5.

Paired rows of experimental Cu deposition in TSV (upper) and computational predictions (lower) for 20 µmol/L, 40 µmol/L, and 80 µmol/L Cl^-, all with 40 µmol/L Tetronic 701, at the indicated potentials. The patterned substrates were rotated at 100 rpm during deposition. Specified deposition times, selected to avoid impingement of growth on the sidewalls while still yielding visible deposits, apply to both experiment and simulation. Parameters for the simulations are found in Table I, with a 25 µm boundary layer thickness appropriate for the experimental rotation rate.

NIST Author Manuscript

NIST Author Manuscript

NIST Author Manuscript

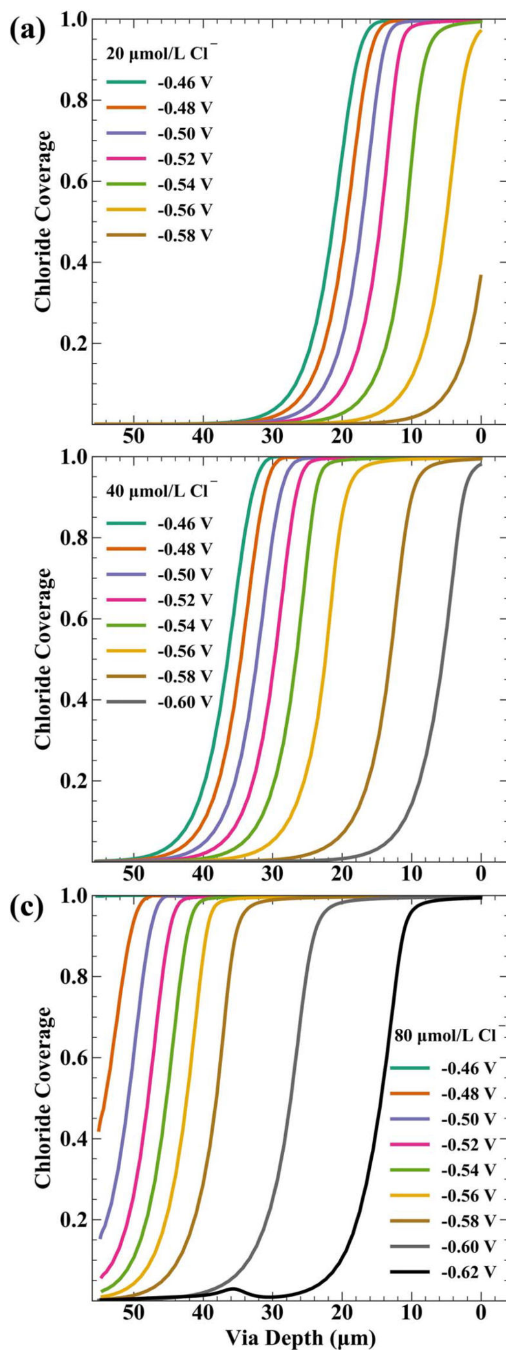

Figure 6.

Predicted chloride coverage along the outer sidewall of the TSV for the indicated potentials and chloride concentrations of a) 20 μmol/L, b) 40 μmol/L and c) 80 μmol/L after 2 minutes of deposition. Parameters for the simulations are found in Table I, with a 25 μm boundary layer thickness appropriate for the experimental rotation rate.

NIST Author Manuscript

NIST Author Manuscript

NIST Author Manuscript

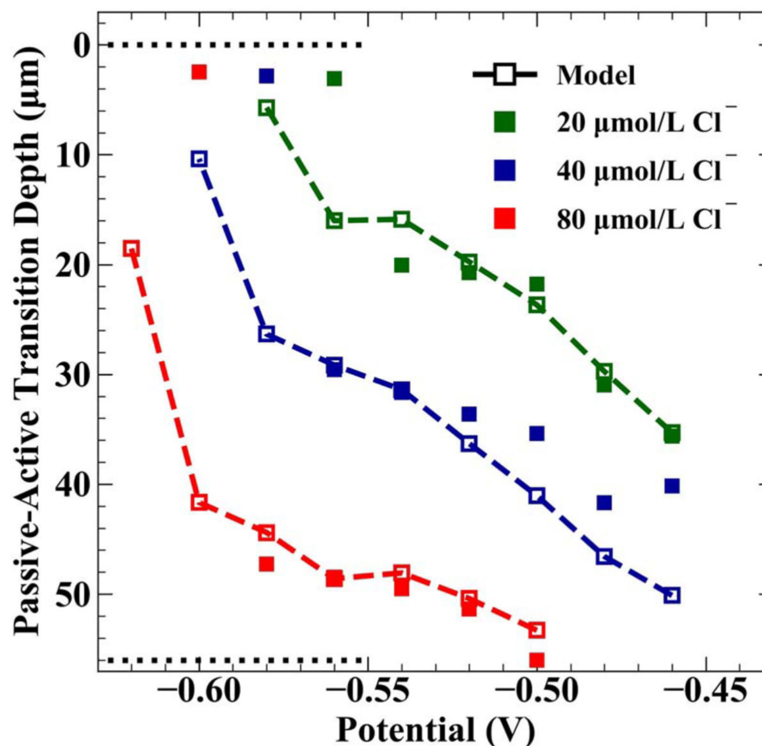

Figure 7.

Experimental values (■) and model predictions (□) of the passive-active transition depth at the indicated chloride concentrations as functions of applied potential (dashed lines are intended only to guide the eye). Experimental values are measured from optical micrographs (Figure 5) and correspond to either the thickest location in the deposit or, for deposits with no obvious maximum, the highest location where the full thickness is achieved. Computational values are analogously defined as either the location of the thickest deposit in the simulation or, for conditions that exhibit no local maximum, the height at which 90% of the maximum thickness is achieved. Experiments and computations are at corresponding times. Dotted lines represent the TSV bounds with zero being at the field. Parameters for the simulations are found in Table I, with a 25 μm boundary layer thickness appropriate for the experimental rotation rate.

NIST Author Manuscript

NIST Author Manuscript

NIST Author Manuscript

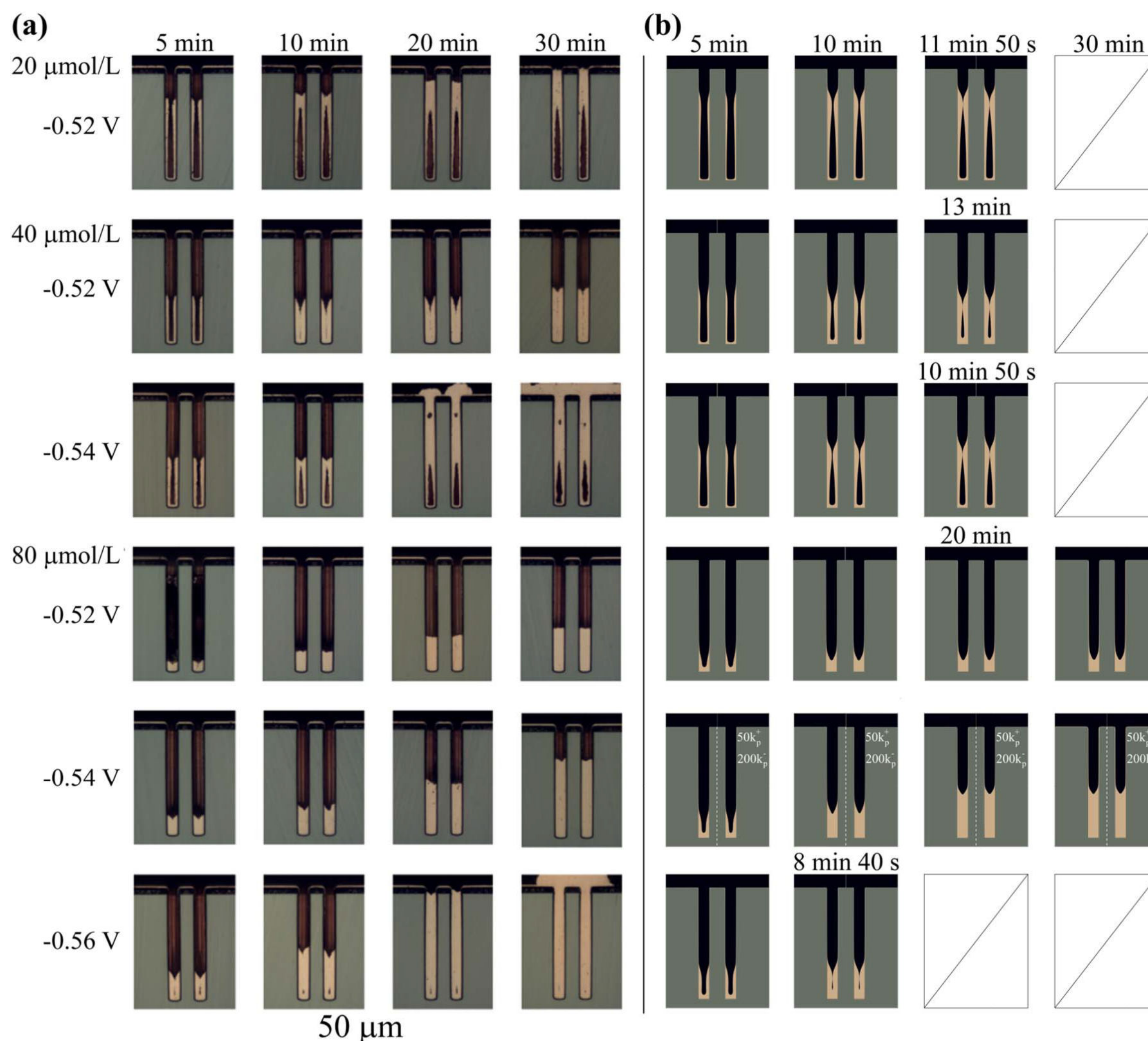

Figure 8.

a) Cross-sectioned annular TSVs and b) computational predictions after deposition for the noted times at the specified applied potentials in electrolytes containing the indicated Cl^- concentrations in addition to 40 µmol/L Tetronic 701. The patterned substrates were rotated at 100 rpm during deposition. Simulations are only shown through sidewall impingement. Parameters for the simulations are found in Table I, with a 25 µm boundary layer thickness appropriate for the experimental rotation rate except for the simulations in the right-hand vias for 80 µmol/L and –0.54 V, which instead use a 50-fold increase in k_p^+ (2500 m^3/mol · s) and 200-fold increase in k_p^- (1×10^7 1/m).

NIST Author Manuscript
NIST Author Manuscript
NIST Author Manuscript

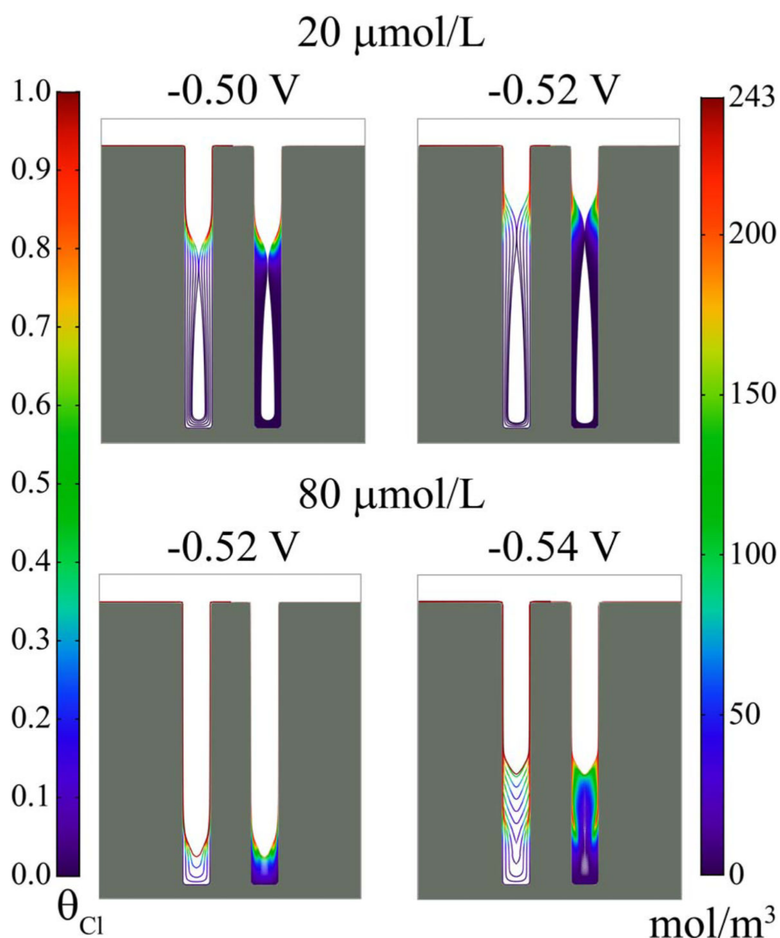

Figure 9.

S-NDR model predictions of chloride coverage (left-hand vias) and concentration maps of chloride incorporated in the deposit (right-hand vias) at the indicated potentials and bulk Cl^- concentrations. Coverage contours for 20 μmol/L Cl^- and 80 μmol/L Cl^- are spaced every 3 min and 2 min, respectively, of deposition. Predictions of chloride concentration in the deposit assume all adsorbed chloride that leaves the surface is incorporated into the deposit. The white lines for the 80 μmol/L Cl^- conditions are artifacts of plotting related to mesh size in the simulations and do not indicate formation of seams or voids.

NIST Author Manuscript

NIST Author Manuscript

NIST Author Manuscript

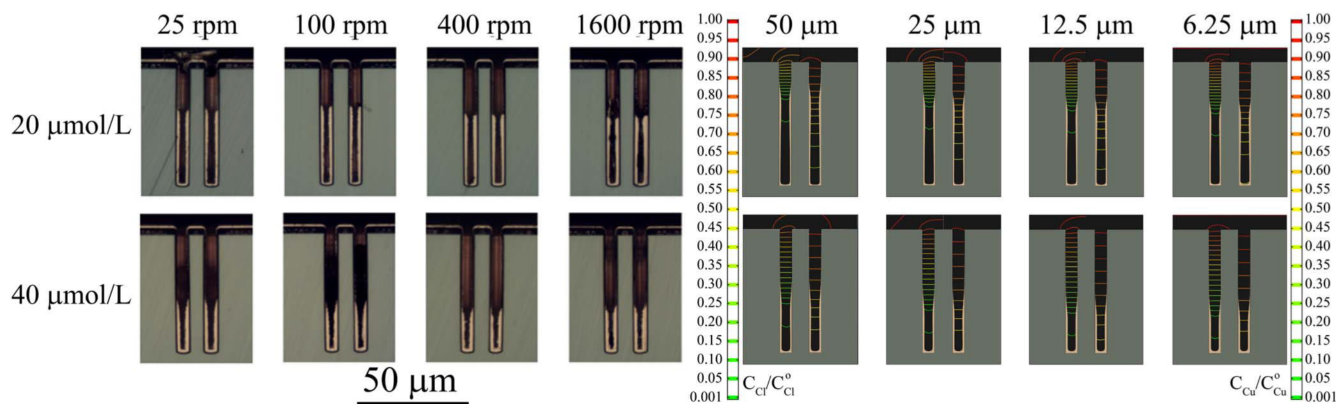

Figure 10.

Cross-sectioned annular TSVs (left half) and corresponding computational predictions (right half) after 5 min of Cu deposition at −0.50 V for the indicated substrate rotation rates and corresponding boundary layer thickness (δ) in electrolyte containing the indicated Cl^- concentrations in addition to 40 µmol/L Tetronic 701. Isocontours of chloride and metal ion concentrations, normalized by the bulk concentrations, are overlaid on the left and right sides, respectively, of the unfilled volume. Parameters for the simulations are found in Table I.

NIST Author Manuscript
NIST Author Manuscript
NIST Author Manuscript

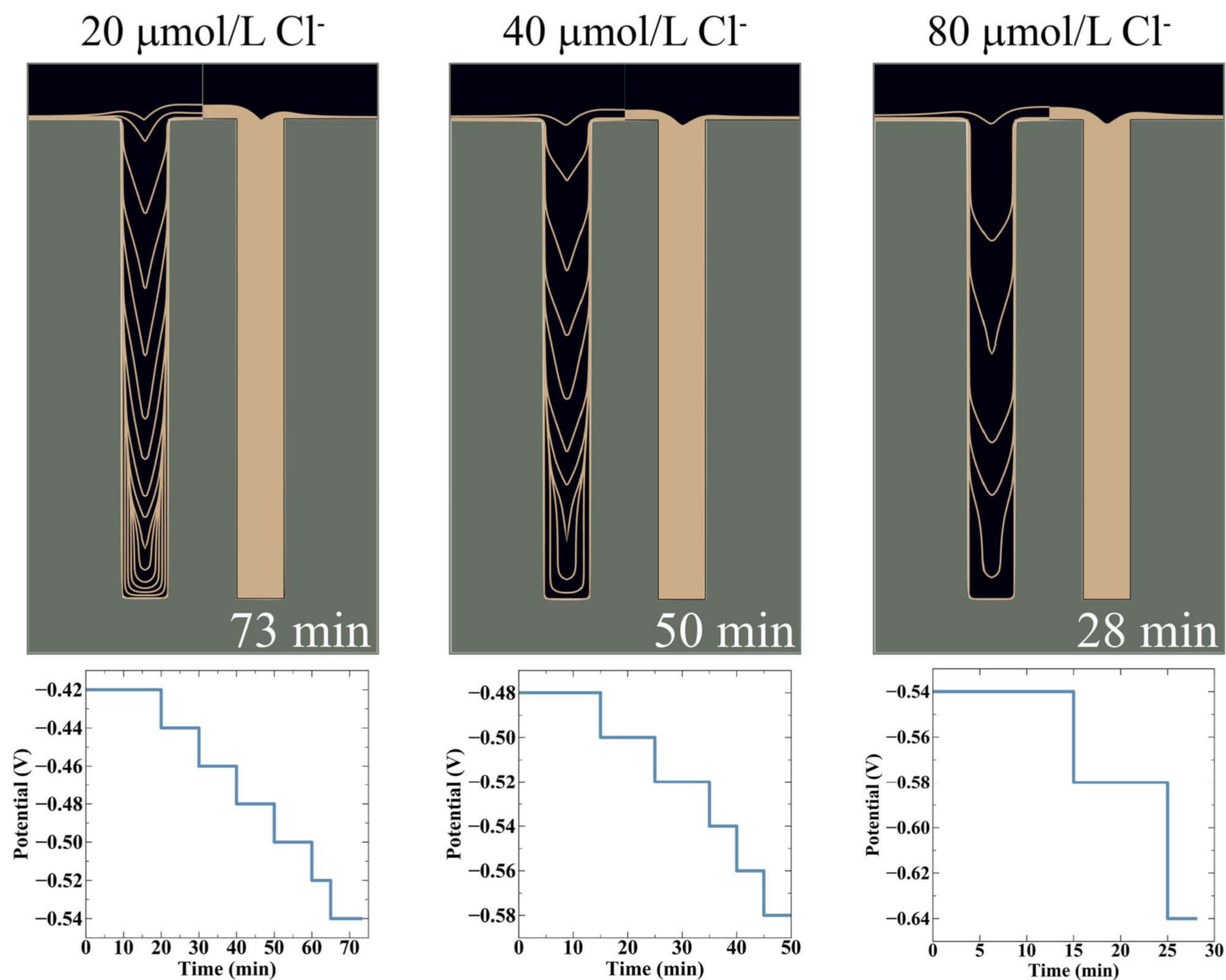

Figure 11.

S-NDR model predictions of Cu feature filling using the potential step waveform shown beneath each simulation for the indicated Cl^- concentrations, each with 40 μmol/L Tetronic 701. Filling contours at 5 min intervals are shown in the left-hand side of each via, with the total deposition time as specified. The interval for the final contour in 20 μmol/L Cl^- and 80 μmol/L Cl^- is 3 min. The right-hand side of each via simply shows filling at the final contour. Parameters for the simulations are found in Table I, with a 25 μm boundary layer thickness appropriate for simulation of a 100 rpm rotation rate.

NIST Author Manuscript
NIST Author Manuscript
NIST Author Manuscript

Table I.

Parameter for voltammetry and feature filling simulations.

Parameter	Name	Units	Value
Annular TSV inner radius	R_i	m	4×10^{-6}
Annular TSV outer radius	R_o	m	9.5×10^{-6}
Simulation cell radius	R_c	m	26×10^{-6}
TSV height	h	m	56×10^{-6}
Distance to reference electrode	L	m	2.5×10^{-3}
Diffusion coefficient[38] Cu^{2+}	D_{Cu}	m^2/s	2.65×10^{-10}
Diffusion coefficient Cl^-	D_{Cl}	m^2/s	9×10^{-10}
Diffusion coefficient[41–43] Tetronic 701	D_P	m^2/s	1×10^{-10}
Diffusion coefficient[39] SO_4^{2-}	D_{SO4}	m^2/s	1.07×10^{-10}
Diffusion coefficient[39] H^+	D_H	m^2/s	9.31×10^{-9}
Diffusion coefficient[39] Na^+	D_{Na}	m^2/s	1.33×10^{-9}
Bulk concentration Cu^{2+}	C_{Cu}^o	mol/m^3	1000
Bulk concentration Polyether	C_P^o	mol/m^3	0.04
Bulk concentration SO_4^{2-}	C_{SO4}^o	mol/m^3	1500
Bulk concentration H^+	C_H^o	mol/m^3	500
Boundary layer thickness for rotation rate $\omega = 200\pi$ rad/min (100 rpm)	δ	m	25×10^{-6}
Saturation chloride coverage	Γ_{Cl}	mol/m^2	1.62×10^{-5}
Saturation suppressor coverage Tetronic 701[44]	Γ_P	mol/m^2	9.2×10^{-8}
Chloride adsorption kinetics	k_{Cl}^+	$m^3/mol \cdot s$	20
Chloride deactivation kinetics	k_{Cl}^-	1/m	1.5×10^7
Suppressor adsorption kinetics	k_P^+	$m^3/mol \cdot s$	50
Suppressor deactivation kinetics	k_P^-	1/m	5×10^4
Unsuppressed Cu exchange current density	j_0^o	A/m^2	20

Parameter	Name	Units	Value
Suppressed Cu exchange current density	j_1^o	A/m^2	0.13
Unsuppressed charge transfer coefficient	α_0	-	0.5
Suppressed deposition charge transfer coefficient	α_1	-	0.5
Cu ionic charge	n	-	2
Cu molar volume	Ω	m^3 /mol	7.1×10^{-6}
Electrolyte conductivity	κ	S/m	15.26
Temperature	T	K	293

NIST Author Manuscript
NIST Author Manuscript
NIST Author Manuscript